Cassini imaging of Saturn: Southern hemisphere winds and vortices

A. R. Vasavada,[1] S. M. Hörst,[1] M. R. Kennedy,[2] A. P. Ingersoll,[3] C. C. Porco,[4] A. D. Del Genio,[5] and R. A. West[1]

[1] High-resolution images of Saturn's southern hemisphere acquired by the Cassini Imaging Science Subsystem between February and October 2004 are used to create maps of cloud morphology at several wavelengths, to derive zonal winds, and to characterize the distribution, frequency, size, morphology, color, behavior, and lifetime of vortices. Nonequatorial wind measurements display only minor differences from those collected since 1981 and reveal a strong, prograde flow near the pole. The region just southward of the velocity minimum at 40.7°S is especially active, containing numerous vortices, some generated in the proximity of convective storms. The two eastward jets nearest the pole display periodicity in their longitudinal structure, but no direct analogs to the northern hemisphere's polar hexagon or ribbon waves were observed. Characteristics of winds and vortices are compared with those of Saturn's northern hemisphere and Jupiter's atmosphere.

1. Introduction

[2] The Cassini spacecraft entered orbit around Saturn on 30 June 2004 and began a 4-year primary mission investigating the planet, its rings, satellites, and magnetosphere. One of the goals of the Cassini Imaging Science Subsystem (ISS) [*Porco et al.*, 2004] is to investigate the structure and dynamics of Saturn's atmosphere by regularly acquiring global image mosaics at wavelengths from the ultraviolet through the near infrared. The potential for new discovery derives from several advantages that the ISS enjoys relative to previous investigations, such as an extended wavelength range including the ultraviolet and narrow CH_4 absorption bands, a sensitive detector, and a multiyear presence in orbit. Atmospheric monitoring began during the spacecraft's approach to Saturn and will continue at planned intervals throughout its mission. Two guiding themes are the search for any seasonal changes and the comparison of Saturn's meteorology with that of the other giant planets, especially Jupiter (which was observed by Cassini in 2000–2001). In this paper and our initial report [*Porco et al.*, 2005] we address these themes with a broad survey of Saturn's atmospheric dynamics, including measurements of the strength, distribution, and other characteristics of zonal jets, vortices, and storms.

[3] The Voyager missions were the first to reveal the detailed morphology and dynamics of Saturn's atmosphere [*Smith et al.*, 1981, 1982; *Ingersoll et al.*, 1984]. Coverage was biased toward the northern hemisphere by the early northern Spring timing and the trajectories of the spacecraft, especially Voyager 2. As the Voyager studies noted, cloud features are harder to detect than at Jupiter due to weaker illumination and differences in atmospheric structure. At Saturn's greater distance from the Sun, temperatures at a given altitude are colder, resulting in lower cloud condensation levels. In addition, Saturn's lower gravity leads to more column mass above a given pressure level, and therefore greater potential for molecular and aerosol scattering. The result is that the appearance of Saturn in the ultraviolet through near infrared is controlled primarily by scattering in a tropospheric haze of many optical depths (of up to several tens of times) that lies above the putative tropospheric cloud deck [e.g., *Muñoz et al.*, 2004; *Temma et al.*, 2005; *Pérez-Hoyos et al.*, 2005; *Karkoschka and Tomasko*, 2005]. There is still significant uncertainty in the vertical structure of Saturn's cloud and haze layers, and the penetration depths of sunlight within various spectral bands used when observing Saturn.

[4] Cloud-tracking studies using Voyager and more recent Hubble Space Telescope (HST) images show that zonal (east-west) jets dominate the dynamics of Saturn's atmosphere [*Smith et al.*, 1982; *Ingersoll et al.*, 1984; *Sánchez-Lavega et al.*, 2000, 2004]. The latitudinal profile of zonal velocity is roughly symmetric across the broad, prograde jet at the equator and has about ten jets in each hemisphere. (Nearly all flow on Saturn is eastward when referenced to the System III rotation rate. Nevertheless, we refer to minima in eastward velocity as "westward jets" in this

[1]Jet Propulsion Laboratory, California Institute of Technology, Pasadena, California, USA.
[2]Department of Geological Sciences, Arizona State University, Tempe, Arizona, USA.
[3]Division of Geological and Planetary Sciences, California Institute of Technology, Pasadena, California, USA.
[4]Cassini Imaging Central Laboratory for Operations, Space Science Institute, Boulder, Colorado, USA.
[5]NASA Goddard Institute for Space Studies, New York, New York, USA.

study.) Recent analyses of HST images acquired between 1996–2004 find slower equatorial wind speeds relative to those measured in 1981 [*Sánchez-Lavega et al.*, 2003, 2004]. However, Cassini multispectral imaging results and thermally derived winds [*Porco et al.*, 2005; *Flasar et al.*, 2005] suggest that wind speeds decrease with altitude in the equatorial region. Therefore some or all of the decrease in measured wind speed may be due to the presence of tracers at higher altitudes rather than a decrease in velocity at a given level. Massive outbursts of new cloud material, such as Saturn's Great White Spots, are one type of phenomena capable of changing the vertical distribution of aerosols over multiyear timescales [*Barnet et al.*, 1992; *Acarreta and Sánchez-Lavega*, 1999].

[5] Images from Voyager, HST, and our initial Cassini report [*Porco et al.*, 2005] show a variety of cloud morphologies, including discrete clouds, vortices, convective storms, and planet-encircling waves (such as the "ribbon wave" and north polar "hexagon"). Vortices exhibit a variety of morphologies and colors, are present in both senses of vorticity (i.e., cyclonic and anticyclonic, depending on whether the vortex rotates in the same or opposite sense as the planetary rotation, respectively), and are observed to drift in longitude, orbit each other, and merge. Eruptions of cloud material occur on local to planetary scales [*Hunt et al.*, 1982; *Sánchez-Lavega et al.*, 1991; *Beebe et al.*, 1992; *Barnet et al.*, 1992; *Porco et al.*, 2005]. Cassini has detected a temporal correlation between storm eruptions and Saturn electrostatic discharges (SEDs), and is expected to reveal the characteristics of Saturnian storms (including the role of moist convection) in greater detail. Ribbon waves refer to periodic meanders in latitude along the boundaries between latitude bands, interpreted to indicate baroclinic instability [*Godfrey and Moore*, 1986]. The most distinctive example was observed near 47°N by Voyager, but tentative detections have been noted at 32°S and 48°S [*Sánchez-Lavega et al.*, 2000]. Kinks in the north polar jet stream that are periodic, fixed in longitude, and that form a hexagon when viewed from above the pole, are thought to be Rossby waves [*Godfrey*, 1988; *Allison et al.*, 1990]. Cassini observations are expected to yield insight into the nature, distribution, and lifetime of all such features described above.

[6] Here we present new analyses of Saturn's southern hemisphere winds and vortices based on Cassini images acquired during its approach and first revolution of Saturn, building upon a recent HST analysis of the southern hemisphere [*Sánchez-Lavega et al.*, 2004] and our initial report. This early phase of Cassini's mission at Saturn occurred just after southern Summer solstice, biasing coverage toward the southern hemisphere and complementing the Voyager results. We focus on understanding the dynamics of zonal winds and vortices of the southern hemisphere down to the pole. We present the first detailed, multispectral maps of the southern hemisphere, new wind measurements of unprecedented accuracy, and the first comprehensive study of Saturnian vortices. Topics that involve Saturn's vertical structure, such as vertical variations in temperature, aerosol properties, or opacity, or the dynamics of the equatorial region or convective storms, are left to other studies. Although we refer to the features that we observe and track as cloud features, it is beyond the scope of this

paper to determine if they are located within a tropospheric haze (tens to hundreds of mbar) or ammonia cloud (1–2 bars) layer. For all geometrical calculations we use the 1-bar pressure level, defined as an oblate spheroid with equatorial and polar radii of 60,268 and 54,364 km, respectively. Throughout this paper we use planetographic latitudes and the System III rotation period (10 hours, 39 min, 22.4 s) and west longitude scale. For a discussion of the revised internal rotation period detected by Cassini (not used here), see *Sánchez-Lavega* [2005].

2. Data and Methods

[7] Cassini ISS images of Saturn's atmosphere are acquired with the goals of measuring atmospheric motions from time-lapse imaging, deriving the vertical structure of cloud and haze layers from spectra, deriving aerosol properties from spectral and polarization information, and studying convection, lightning, and aurora. A subset of the atmospheric imaging sequences, including those used here for dynamics, are designed to simultaneously address dynamics and structure following the successful approach used by the Galileo and Cassini imaging teams at Jupiter [*Belton et al.*, 1996; *Vasavada et al.*, 1998; *Banfield et al.*, 1998; *Porco et al.*, 2003]. Image mosaics are taken at regular time intervals using a set of filters at ultraviolet, visible, and near-infrared wavelengths that include both continuum regions and gaseous absorption bands.

[8] Two sets of Cassini imaging data are used in this study, one acquired during the spacecraft's final approach to Saturn and one acquired during its first revolution. The ISS acquired global, multispectral mosaics of Saturn between 6 February and 12 May 2004, continually at intervals of roughly 21 hours (two Saturn rotations) as Cassini approached Saturn. Each global mosaic was constructed by viewing Saturn's disk with the narrow-angle camera at six equally spaced intervals (1 hour 45 min, or ∼60° longitude) during one Saturn rotation. The spatial resolution of the approach images increased gradually from 425 km pixel^{-1} to 155 km pixel^{-1}. The viewing and illumination geometries permitted well-lit views of the southern hemisphere including the pole. The subspacecraft latitude was 19.8°S, the solar phase angle was ∼65°, and the subsolar latitude was ∼30°S. The northern hemisphere was obscured from view by the Saturn-spacecraft geometry, the rings, their shadows, and the low seasonal illumination. Future Cassini observations will have better views of the northern hemisphere.

[9] The ISS acquired higher-resolution images of Saturn's southern hemisphere between 6 September and 15 October 2004, during Cassini's first revolution. Multispectral mosaics were acquired at irregular intervals (gaps of several days are present). Spatial resolution of the narrow angle camera increased from 53.2 to 27.9 km pixel^{-1}. Complete spatial coverage of the southern hemisphere was achieved by imaging a 2 × 2 grid at each of seven equally spaced longitude intervals (1 hour 30 min, or ∼51° longitude) during a rotation of Saturn. The viewing and illumination geometries were similar to those during the approach movie. The subspacecraft latitude ranged from 20.4°S to 16.2°S, the solar phase angle ranged from 83.8° to 65.4°, and the subsolar latitude was ∼29°S. For wind measurements, we

searched this data set for pairs of mosaics with global coverage and a time separation of only one rotation. The latest (and therefore highest resolution) pair was acquired on 18–19 September 2004. These images have a spatial resolution of 49.6 km pixel^{-1}.

[10] The ISS narrow-angle camera (wide-angle images were not used here) initially records 12-bit data numbers (DNs) for 1024 × 1024 pixels. DNs of images used in this study were reduced to eight bits using an optimized square-root function. Huffman compression (lossless) was used for transmission to Earth. The physical and operational parameters of the ISS are described by *Porco et al.* [2004]. Raw images were processed into maps prior to analysis. The camera geometric model and the photometric calibration software (CISSCAL) are described by *Porco et al.* [2004]. Spacecraft and planetary ephemerides and commanded camera orientations are taken from kernels produced by the Navigation and Ancillary Information Facility (NAIF) at the Jet Propulsion Laboratory. For images containing an illuminated planetary limb, camera (i.e., spacecraft) pointing errors were removed by fitting a calculated limb to the image data. Only one of the four frames in the 2 × 2 pattern of higher-resolution images contained a navigable limb. The remaining three were navigated to the limb frame by correlating the overlapping regions. Navigated frames were mapped to a simple cylindrical (rectangular) projection, with equal increments of planetocentric latitude and longitude on the axes. We used a map scale of 0.1° pixel^{-1} (~105 km pixel^{-1} at the equator) for all of the work described in this paper except the wind measurements, for which we used a map scale of 0.05° pixel^{-1} in order to retain more of the detail present in the raw images (in other words, the effective resolution of the maps differed from that of the raw images, which varied between 425 and 27.9 km pixel^{-1}).

[11] The methods described thus far closely follow those used in our previous analyses of Galileo and Cassini imaging data of Jupiter [*Vasavada et al.*, 1998; *Porco et al.*, 2003, 2005]. Removing solar illumination on Saturn images required a novel approach to photometric correction. The purpose of a photometric correction is to remove the dynamic range arising from illumination variations in order to emphasize the contrast within cloud features; cloud features with lower intrinsic contrast therefore require highly accurate illumination corrections. Simple photometric functions (i.e., Minnaert) are inadequate because of scattered sunlight from Saturn's rings. Facing these complexities, we chose to flatten the images using a high-pass filter. The filter box size of 7.5° × 7.5° assures that information relevant to our study is preserved, namely the shape and spatial structure of cloud features and vortices, while spatially large variations in brightness due to direct and indirect solar illumination are removed. Some latitudinal variation in albedo is unavoidably lost. After correction for illumination, the frames were assembled into global maps using an average weighted by emission angle where images overlapped. Because each map contains data acquired over many hours, wind speeds were calculated using the acquisition times of the individual frames. Navigation, map projection, illumination correction, and wind measurements were accomplished using custom software written in the Interactive Data Language (IDL).

[12] The approach maps (hereafter called AMs) were acquired in six filters: BL1 (451 nm), GRN (568 nm), MT1 (619 nm), CB1 (619 nm, straddling the CH$_4$ absorption band), MT2 (727 nm), and CB2 (750 nm). The two higher-resolution maps used for wind measurements (hereafter called HRMs) were acquired in those filters except GRN, and in UV3 (338 nm), MT3 (889 nm), CB3 (938 nm). The numbers in parentheses are the central wavelengths of the ISS system transmission through the filter. The choice of filter band pass varied depending on whether the purpose was broadband color (UV3, BL1, GRN), near-infrared continuum measurements (CB1, CB2, CB3), or sounding within a CH$_4$ absorption band (MT1, MT2, MT3) [*Porco et al.*, 2004]. For most of the work described below we use images in the near-infrared continuum region (CB2), where Rayleigh scattering and gaseous absorption are minimized, permitting reflections from features deeper in Saturn's troposphere, relative to other wavelengths.

[13] There are a total of 85 AMs. Some maps or portions thereof are missing due to transmission errors. When possible we substituted CB1 for missing CB2 images (differences are minimal). Even so, five of the AMs have one or more missing longitude segments, while two are entirely missing. There are two HRMs. A region of 50° longitude is missing from the second map.

3. Appearance and Zonal Winds

[14] Cloud morphologies in the HRM of Saturn's southern hemisphere (Figures 1 and 2) resemble the Voyager and HST descriptions of zonal bands, discrete clouds, vortices, and convective storms. Figure 3 shows the relationship between the appearance and zonal winds. The equatorial region (0°–10°S) contains diffuse and patchy brightness variations and small cloud streaks, in contrast with the more sharply defined cloud patterns seen at other latitudes. This appearance is consistent with the presence of an upper tropospheric haze that is higher and optically thicker in the equatorial region [*Muñoz et al.*, 2004; *Temma et al.*, 2005; *Pérez-Hoyos et al.*, 2005; *Karkoschka and Tomasko*, 2005]. A pattern of tilted cloud streaks covers latitudes between 10°S and 29.5°S, revealing the strong latitudinal shear in the zonal winds. The region between 29.5°S and 33°S contains a set of peculiar features, quasiperiodic in longitude and extending around the planet. At some longitudes the pattern appears similar to a Karman vortex street [*Godfrey et al.*, 1983; *Ingersoll et al.*, 1984], while at others it resembles a pair of wavy cloud streaks that pinch and separate over longitude, each similar to the northern hemisphere ribbon wave [*Godfrey and Moore*, 1986; *Sánchez-Lavega et al.*, 2000]. The feature probably results from the interaction between a pair of narrow zonal jets at 31°S and 33°S.

[15] Tilted cloud streaks are present from 33°S to 38.5°S. The region between 38.5°S and 46°S, the peak and poleward side of the broad westward jet centered near 41°S, is distinguished by an abundance of vortices. Vortex-related cloud filaments and patchy bright clouds fill the area between vortices. This region is also associated with active but short-lived (days to weeks) convective outbursts, such as the bright storm seen in Figure 3 and described by *Porco et al.* [2005]. Because of its relative high activity, the region
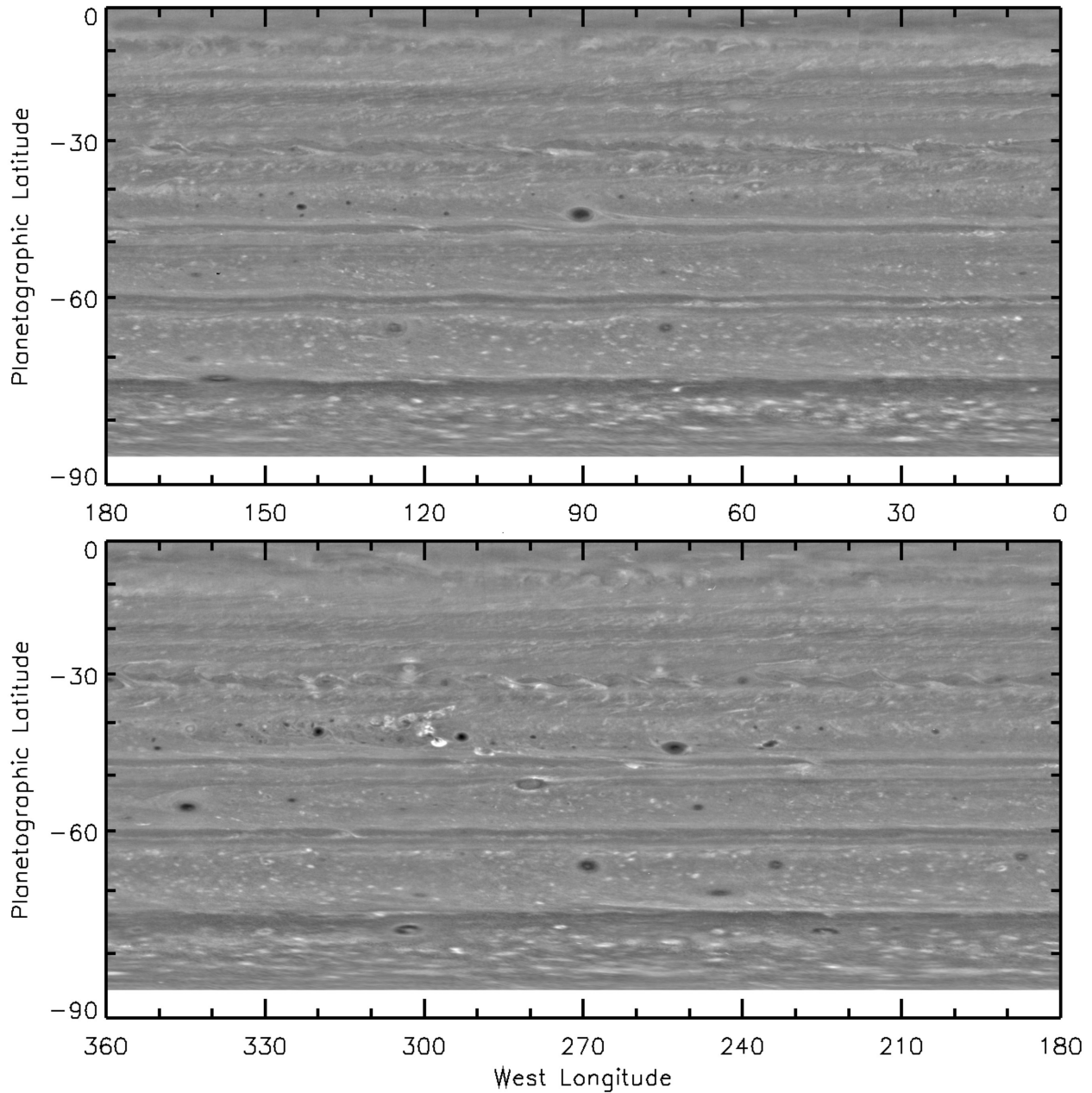
Figure 1. Cylindrical map projections of Saturn's southern hemisphere on 18 September 2004, during Cassini's first revolution of the planet. The map shown here is the first of the HRM pair used for wind measurements. The spatial resolution of the raw 750-nm images is ∼50 km pixel^{-1} in the image plane. The map is split into two longitude segments for clarity. Latitudes near the pole are omitted here and shown with less distortion and better photometric correction in Figure 4. Note that illumination effects were removed using a high-pass filter.

has been referred to as "storm alley" in Cassini public releases. A pair of dark bands straddles each of the eastward jets near 49.5°S and 60.5°S. The former band pair is wider (4.5° latitude) than the latter (3°). A narrow, brighter band is located near the peak of the jet. The regions between these dark band pairs (including another near the eastward jet at 74.5°S) are relatively wider bands containing vortices and patchy bright clouds.

[16] The south polar map (Figure 2) indicates no obvious southern analog to the north polar hexagon near 78.5°N

[*Allison et al.*, 1990; *Sánchez-Lavega et al.*, 2002]. However, the dark band pair containing the 60.5°S jet does have a polygonal appearance over 120° of longitude, with four nodes separated by ∼30° of longitude (suggesting a wave number 12 structure). The structure is ephemeral; images acquired several days before and after the HRM do not show the same pattern. The dark band containing the 74.5°S jet also has a faint polygonal structure, with tilted bright cloud streaks extending equatorward at intervals of 45°−60° of longitude (like a pinwheel). The pole itself is a dark spot surrounded by a

Figure 2. Polar stereographic projection of Saturn's southern hemisphere on 18 September 2004, during Cassini's first revolution of the planet. The map shown here is the first of the HRM pair used for polar wind measurements. The spatial resolution of the raw 750-nm images is ~50 km pixel^{-1} in the image plane. Data within 10° latitude of the pole are taken from a single mapped image.

ring of bright cloud material at 88.8°S. The dark spot is reminiscent of the infrared hot spot described by *Orton and Yanamandra-Fisher* [2005]. The polar cloud ring is slightly off center from the pole (not due to viewing geometry) and contains a small segment of arc with increased width.
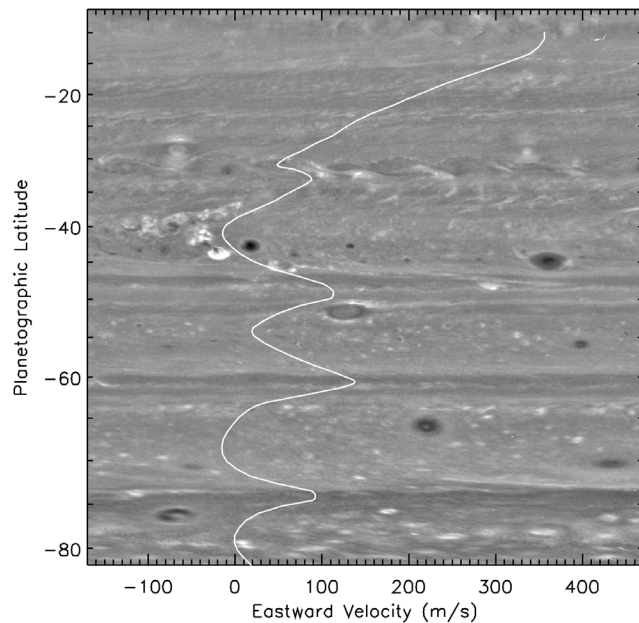

Figure 3. Profile of Saturn's zonal winds measured on Cassini images overlain on a segment of the cylindrical map shown in Figure 1.
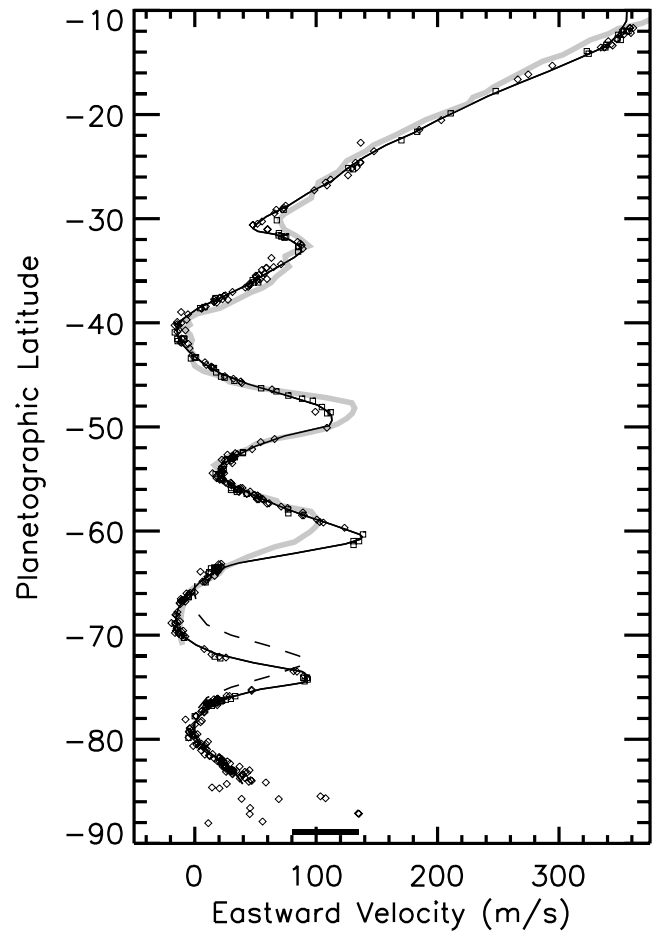

Figure 4. Plot of the 458 Cassini zonal wind measurements from this study and *Porco et al.* [2005]. The thin solid curve has been manually fit to the Cassini points. Voyager (thick shaded curve) [*Sánchez-Lavega et al.*, 2000] and HST (dashed curve) [*Sánchez-Lavega et al.*, 2002] profiles are shown for comparison. The box near the pole bounds the velocities of features on a circumpolar cloud ring ~3° in diameter.

[17] We measured the latitudinal profile of zonal wind by tracking the displacement of cloud features on the pair of HRMs. The time separation is 10 hours 30 min, giving a precision of 1.4 m s^{-1} for a displacement of one map pixel at the equator. The combination of errors due to image navigation, feature tracking, and foreshortening at higher latitudes is estimated to be <20 pixels (consistent with the low dispersion of the measurements shown below). Features were identified and tracked by eye using custom IDL software that blinks the mapped images on a monitor and allows the user to fine-tune tiepoint locations on a pair of static zoom windows. Tracked features include discrete clouds and long-lived morphological features (e.g., kinks) within cloud bands or streaks. Vortices, diffuse clouds/hazes, and features that exhibited nonzonal motions were avoided in order to derive the ambient flow with the highest accuracy. At any given location, cloud features appear to translate with a single wind speed; no evidence of multilevel cloud decks or vertical wind shear was found in the CB2 images.

[18] Figure 4 shows a total of 458 wind measurements, including 347 on the HRMs from our study and 111 on the

AMs first shown by *Porco et al.* [2005] (using similar methods and software). Figure 4 also shows a manually constructed, best fit curve that represents the details of the wind profile better than one constructed by binning or averaging the irregularly spaced measurements. Wind measurements and our best fit curve are available electronically as auxiliary material[1]. Figure 4 shows that there are differences between this curve and those constructed from Voyager and HST measurements [*Sánchez-Lavega et al.*, 2000, 2002, 2004]. The eastward jet near 49.5°S is ∼20 m s^{-1} slower during the Cassini era, while the eastward jet near 60.5°S is 35 m s^{-1} faster. The jet shape and latitude also differ in both cases. The large discrepancy in the latitude of the 74.5°S eastward jet is not understood. However, our measurements follow the Voyager measurements just equatorward of the jet, while the HST measurements differ from both. The differences in the zonal velocity profile noted above may indicate real changes in jet speeds. However, we cannot say with confidence that their magnitude exceeds the error when comparing measurements from several authors, data sets, and techniques (not to mention that introduced by the tracers and their variation over time). Several types of error are accentuated at jet peaks and high latitudes. The best test of the robustness of our measurements will be when the Cassini data are analyzed by other workers.

[19] In order to facilitate high-latitude wind measurements, the raw images that comprise the HRMs were individually mapped in polar stereographic projection. Cloud tracking was performed on these maps from 73.5°S to the pole. Measurements from the cylindrical and polar maps are indistinguishable where they overlap. The polar wind measurements (Figure 4) exhibit little dispersion equatorward of ∼84°S. Poleward of that latitude, measurements are all positive (eastward), but vary between 0 and 140 m s^{-1}. Figure 2 reveals the lack of discrete cloud features at these latitudes that makes measuring winds difficult. Tracking the asymmetric bright ring that surrounds the pole at 88.8°S provided a set of very high-latitude measurements that fall between 80 to 135 m s^{-1}. There is an ambiguity in whether the latter measurements refer to the ambient flow or the phase speed of a wave structure.

[20] Figures 5a and 5b illustrate the appearance of Saturn's southern hemisphere at six of the eight wavelengths used to acquire the HRM data set (CB1 and CB3 are excluded as they are very similar to CB2). Model-based vertical retrievals are beyond the scope of the present work, but we make some qualitative statements here and in section 4.4. First we review what each wavelength band is expected to reveal, consistent with the most recent work on cloud and haze stratigraphy [*Muñoz et al.*, 2004; *Temma et al.*, 2005; *Pérez-Hoyos et al.*, 2005; *Karkoschka and Tomasko*, 2005]. Images in BL1 sense relatively deeply but are sensitive to color variations in the cloud/haze layers (i.e., particle absorption), as well as Rayleigh scattering by gas. Images in red and near-infrared wavelengths may be sensitive to both particle absorption and differential absorption by methane gas. Since methane is uniformly mixed, differential methane absorption is produced by variations in haze
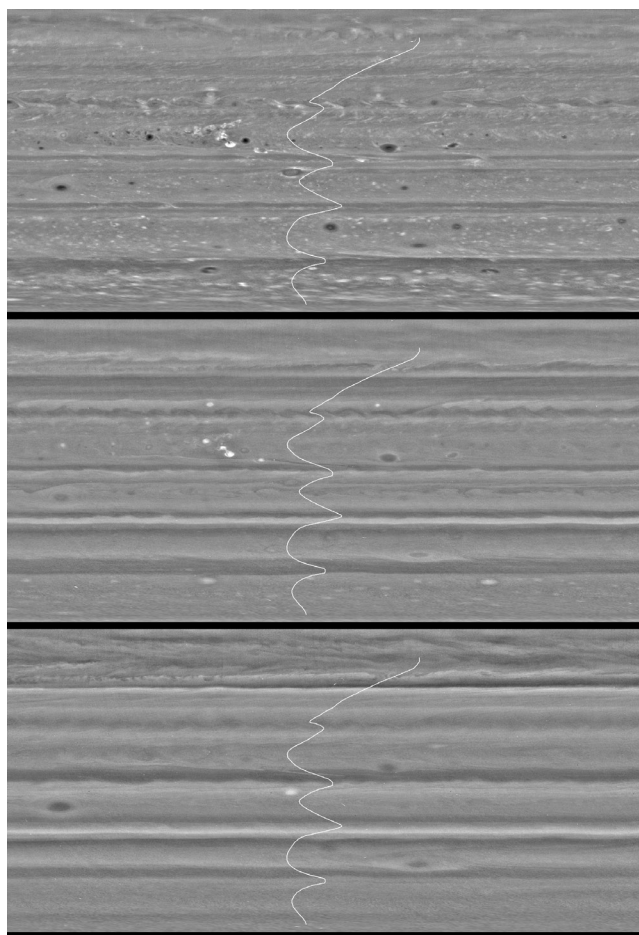

Figure 5a. Appearance of Saturn's southern hemisphere at different wavelengths. Cylindrical maps were constructed from images using (top) the ISS near-infrared continuum filter (CB2, 750 nm), (middle) blue filter (BL1, 451 nm), and (bottom) ultraviolet filter (UV3, 338 nm). Each plot shows longitudes 180°−360°W and latitudes 0°−85°S and is overlain with the Cassini best fit profile of zonal winds (plotted with 0 m s^{-1} at the center). Images at each footprint were acquired within minutes of each other during the collection of the first HRM (i.e., the CB2 map shown here and in Figures 1−3). Very small bright clusters or streaks may be cosmic-ray-induced artifacts on the SSI detector. Note that illumination effects were removed using a high-pass filter.

particle altitude, number density, or scattering cross section. While differential methane absorption dominates in the MT3 filter, the relative importance of particle versus gas absorption becomes less clear in the weaker methane band (MT1 and MT2) and in the continuum bands (CB1, CB2, and CB3).

[21] Of those presented in Figures 5a and 5b, the CB2 filter sounds the deepest and is least affected by gas scattering. Images in the three methane absorption bands (MT1, MT2, and MT3) may be thought of as cutting horizontally through the atmosphere at increasingly higher altitudes. Light at these wavelengths is reflected preferentially from features higher in the atmosphere, above more of
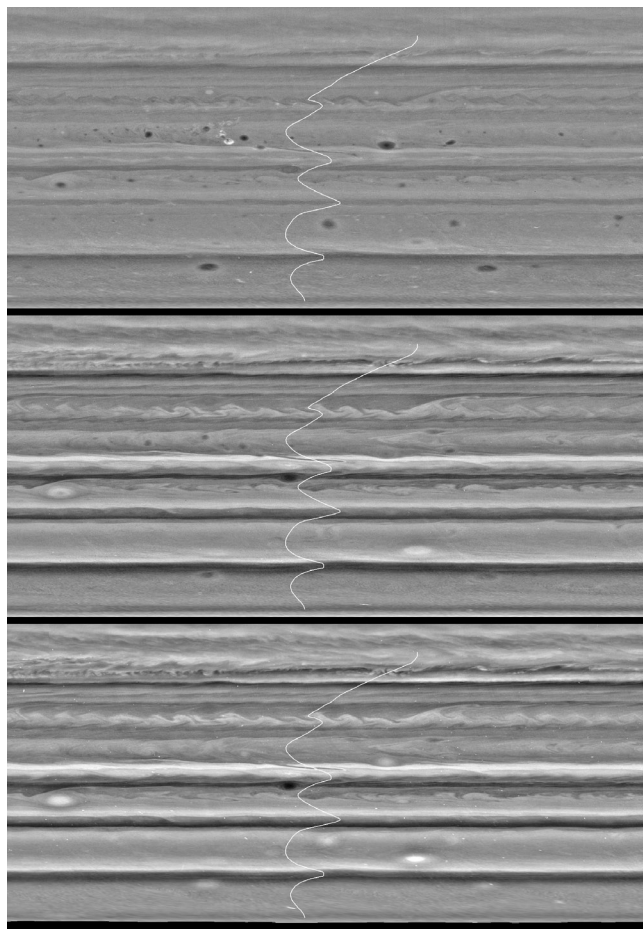
Figure 5b. Similar to Figure 5a, but maps were constructed from images acquired using the three ISS filters centered in progressively stronger CH_4 absorption bands: (top) MT1 (619 nm), (middle) MT2 (727 nm), and (bottom) MT3 (889 nm).

the absorbing gas. In MT3, high-altitude features appear bright against the dark background of absorbing gas. Saturn's appearance in UV3 will expose any ultraviolet-absorbing aerosols and is strongly affected by gas scattering. In UV3, high-altitude features that absorb UV light appear dark against a bright background, since there is less gas above them to scatter light toward the spacecraft. The suite of filters is expected to reveal features at pressure levels between tens and hundreds of mbar.

[22] The CB2 map contains more fine-scale structure than the others in Figures 5a and 5b, such as the internal structure of larger vortices, the presence smaller vortices and patchy clouds, and the convective storm and its associated clouds. In images using filters sensitive to higher features, the contrast between major latitude bands increases, but there is less fine-scale detail. However, when MT images are viewed at full spatial resolution, the bands are found to contain extended cloud filaments that bend and fold due to interactions between jets, or between jets and vortices. In general, there are no major features (e.g., vortices) that are unique to the higher-sounding wavelengths. An important exception occurs near the equator, where there is relatively sharp detail in MT2 and MT3 (and inverted in brightness in

UV3) that is distinct from cloud textures within CB2 at the same location. The presence of distinct and different cloud morphologies in the CB2 and MT2 images allowed the direct measurements of vertical wind shear reported in *Porco et al.* [2005]. The convective storm is not visible in MT2, MT3, or UV3, suggesting that it does not penetrate beyond the deeper levels sensed.

[23] Saturn's banding is correlated with the profile of zonal winds, but not in a way that obviously implies the "belt/zone" model, in which bright anticyclonic regions (zones) signify the upwelling branches of meridional circulations and clear cyclonic regions (belts) are sites of subsidence [*Smith et al.*, 1981]. Figures 5a and 5b show that narrow bands with less cloud/haze scattering occur just southward (i.e., on the cyclonic sides) of the eastward jet maxima at 49.5°S, 60.5°S, and 74.5°S. The two broad regions in between these eastward jets are relatively uniform in brightness, despite the change in sign of vorticity across the westward jet. The region in between the eastward jets at 33°S and 49.5°S conforms more to the belt/zone model, with more scattering from anticyclonic latitudes and less from cyclonic. The band just south of 60.5°S is unusually bright in BL1 and UV3, suggesting low aerosol opacity and enhanced Rayleigh scattering. Finally, the polar spot is dark at all wavelengths except UV3, where it is absent.

4. Vortices

[24] We have analyzed the characteristics and behavior of vortices by measuring their sizes, shapes, and spatial distribution on the HRMs and monitoring their evolution on the AMs. A vortex was noted if it was present in three consecutive AMs or in both HRMs. There were many small, shorter-lived features, but these could not be distinguished from image artifacts. We manually measured the center location, east-west extent, and north-south extent of each vortex using a display tool that allows zooming and adjustment of brightness and contrast. We estimate the uncertainty in the center location to be <2 pixels based on frame-to-frame repeatability and repeated measurements on the same frame. Our approach to determining the center location is similar to that of *Li et al.* [2004]. For symmetric vortices, we estimated the center pixel; for asymmetric vortices, we estimated the centroid of the area of greatest contrast.

4.1. Number and Size Frequency Distribution

[25] The number of vortices counted in the AMs increased with time, primarily as a result of the threefold increase in spatial resolution as the spacecraft approached Saturn. Even the final AMs contain only ∼65 vortices, compared to 138 in the HRMs. The size frequency distributions in Figure 6 suggest that the population of vortices with east-west diameters <1000 km cannot accurately be counted in the final AM. Therefore the AMs cannot reveal how the total number of vortices over all sizes varied with time. However, a comparison of the AM and HRM histograms suggests that the number of mid to large vortices evolved but remained similar between the two observations.

4.2. Vortex Characteristics

[26] We have attempted to classify vortices into families based on their brightness and morphology at 750 nm (CB2
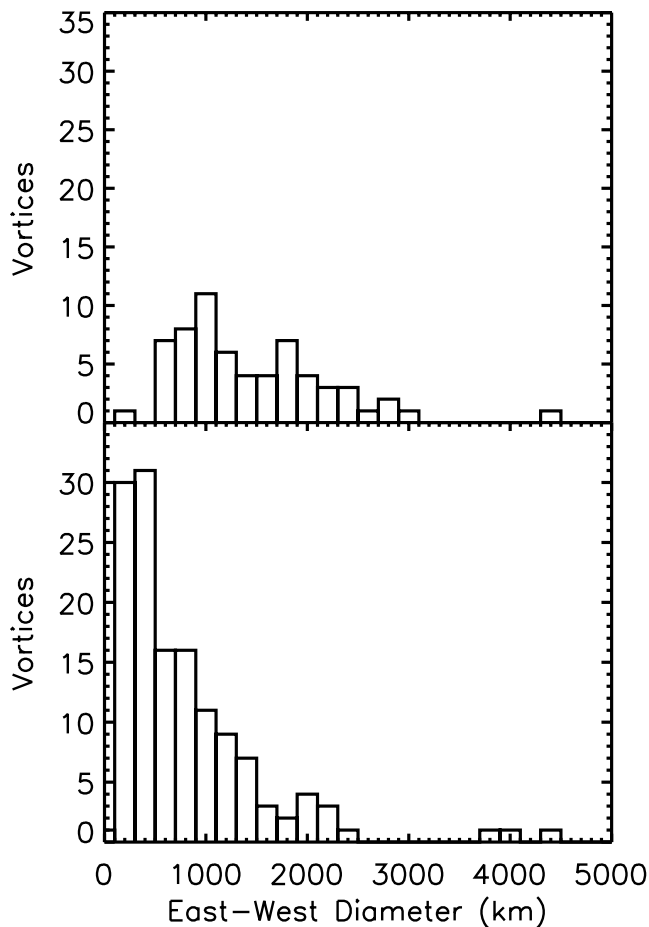
Figure 6. Histograms showing the number of vortices observed of a given east-west diameter (top) on the final approach map and (bottom) during Cassini's first revolution of Saturn. Vortices with diameters less than ∼1000 km were not well resolved in the approach movie images. Larger vortices had a similar size frequency distribution in both data sets, but the sizes of individual vortices have evolved.

filter). Figure 7 shows examples from each of four families: dark, dark with a bright margin, bright centered, and bright. Figures 8 and 9 reveal how the families correlate with latitude, vortex size, and vortex shape. Dark vortices are small, round, numerous, and occur in several latitude bands. Dark vortices with bright margins are larger than dark vortices, but occur in some of the same latitude bands. The largest examples are oval-shaped (extended in the east-west direction). Bright-centered vortices are moderately sized and occur in two latitude bands. Several bright-centered vortices have the unusual property that their north-south diameters exceed their east-west diameters (see Figure 2). There are only two bright vortices, sharing the same latitude band. Six vortices did not easily fit into the above families. These include the largest vortex we observed and a pair of vortices that were caught merging in the HRMs, both shown in Figure 7. Other unclassified vortices include two at 76.4°S that are difficult to differentiate from the ubiquitous patchy clouds, and two bright vortices with unique morphologies at (41.1°S, 344.3°W) and (39.2°S, 57.4°W) in the HRM.

4.3. Relationship to Zonal Winds and Convective Storms

[27] The relationship between zonal wind speed, the sign of the zonal wind shear (i.e., vorticity), and occurrence of vortices is shown in Figure 10. Direct measurement of the tangential velocity within vortices proved difficult (note the lack of azimuthal structure in Figure 7), but their sense of rotation may be inferred (though not definitively) from the shear in which they are embedded. Vortices are clustered in latitude but are present in regions of both cyclonic and anticyclonic shear in the zonal wind. The greatest concentrations of vortices occur near the westward jets, as observed on Jupiter [Li et al., 2004]. Although their frequency is greater within regions of anticyclonic shear, there are several vortices covering a wide range of sizes in regions of cyclonic shear.

[28] Comparing Figure 10 with Figure 8, we can make some inferences about how our vortex families correlate
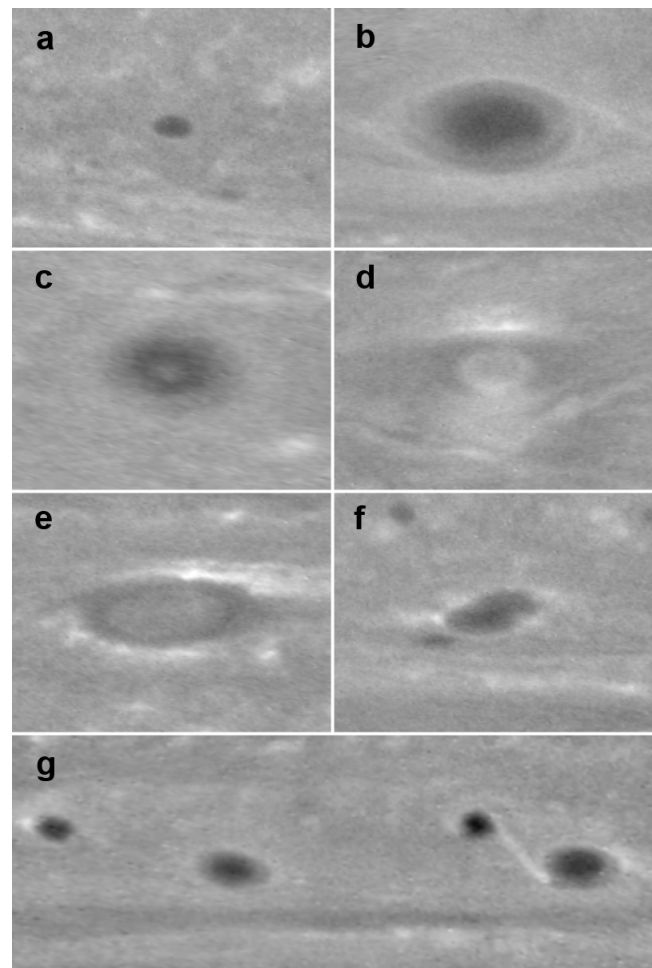

Figure 7. Mosaic showing the variety of vortex brightness and morphology. Vortices are classified into four families: (a) dark, (b) dark with a bright margin, (c) bright centered, and (d) bright. (e) Largest vortex observed on Saturn (4500 km), located at 51.8°S. (f) Two vortices in the process of merging. (g) Two pairs of vortices near 43.4°S connected by an extended filament (8000 km for the left pair) after near misses.
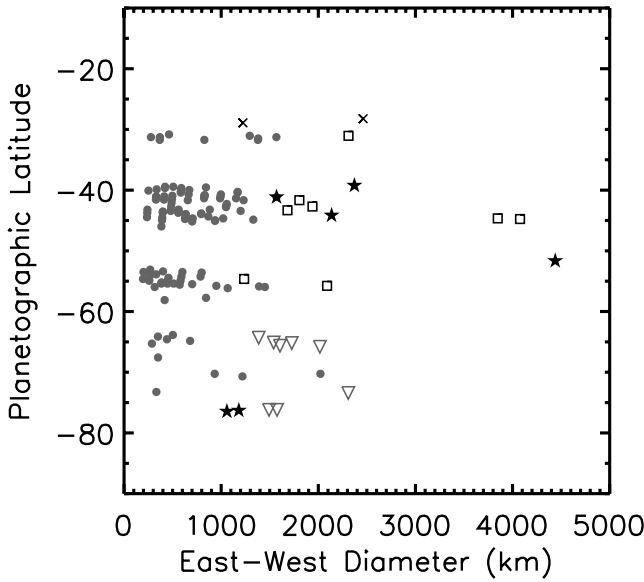
Figure 8. Latitudinal distribution of vortex sizes and types. Vortices are classified as dark (circles), dark with a bright margin (squares), bright centered (triangles), and bright (crosses). Unclassified vortices are plotted as stars.

with the sense of vorticity in the ambient wind. Dark vortices are present in both anticyclonic and cyclonic regions. Dark vortices with bright margins occur only in anticyclonic regions. All but one of the bright-centered vortices are in cyclonic regions, and the exception at 73.5°S does not have the same shape as the others, suggesting that it may be unique. Both of the bright vortices are in a cyclonic region, while the largest vortex we observe (at 51.8°S) is in a cyclonic region.
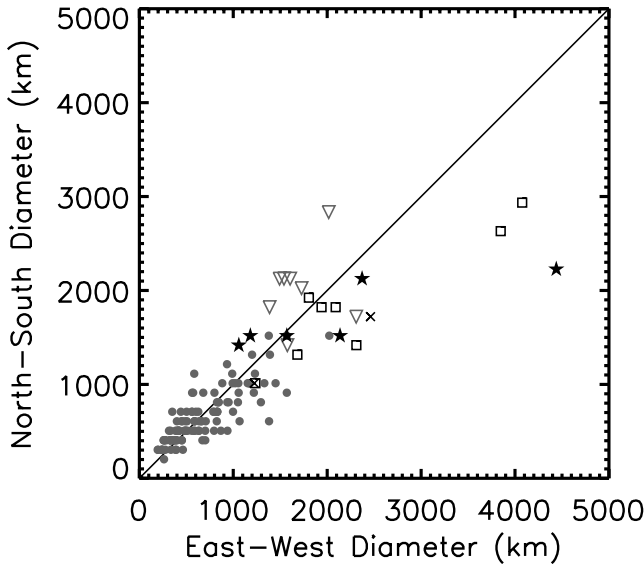

Figure 9. Distribution of vortex shapes and types. Vortices are classified as dark (circles), dark with a bright margin (squares), bright centered (triangles), and bright (crosses). Unclassified vortices are plotted as stars. Symbols falling on the line would indicate circular vortices.
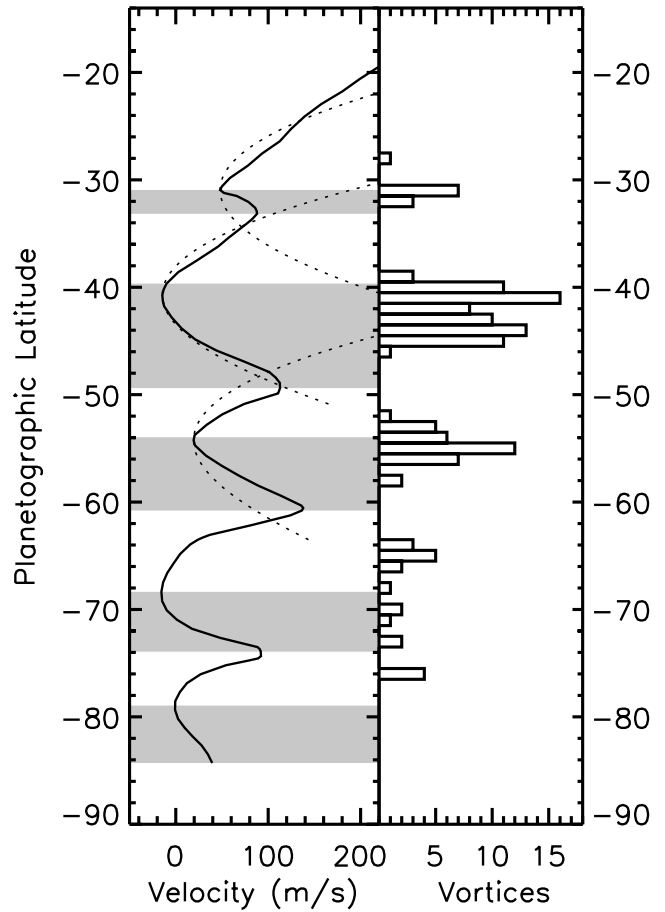

Figure 10. Profile of zonal winds and vortex latitude-frequency histogram. The solid curve is a manual fit to the Cassini zonal wind measurements. The dotted parabolas are centered on the three lowest-latitude westward jets and have curvatures equal to the gradient in planetary vorticity. Where the measured profile lies inside the parabola, the flow violates the barotropic stability criterion. The histogram contains the 138 vortices measured in the high-resolution maps. Shaded (unshaded) regions contain anticyclonic (cyclonic) shear in the zonal winds.

[29] Figure 10 also compares the curvature of the mean zonal wind profile, $d^2\overline{u}/dy^2$, to the planetary vorticity gradient, β. Here $\overline{u}$ is the mean zonal wind speed and y is northward distance. In the framework of two-dimensional flow, jets are stable to barotropic instabilities when their curvature is less than β. The presence of deeper flows may stabilize jets with larger surface-measured curvatures. If instabilities do occur, they can lead to vortex generation [*Dowling and Ingersoll*, 1989]. We find that the curvatures of the westward jets centered near 31°S, 41°S, and 54°S are approximately 5β, β, and 3β, respectively (similar measurements were performed by *Smith et al.* [1981] and *Sánchez-Lavega et al.* [2000]). Vortices are present near each of these locations where the criterion is violated, but the region with the most activity ("storm alley") violates the criterion the least. The relevance of the barotropic stability criterion is unclear, given our lack of knowledge of Saturn's deep winds. However, an important fact is that Saturn's jets, both westward and especially eastward, are sharply peaked.
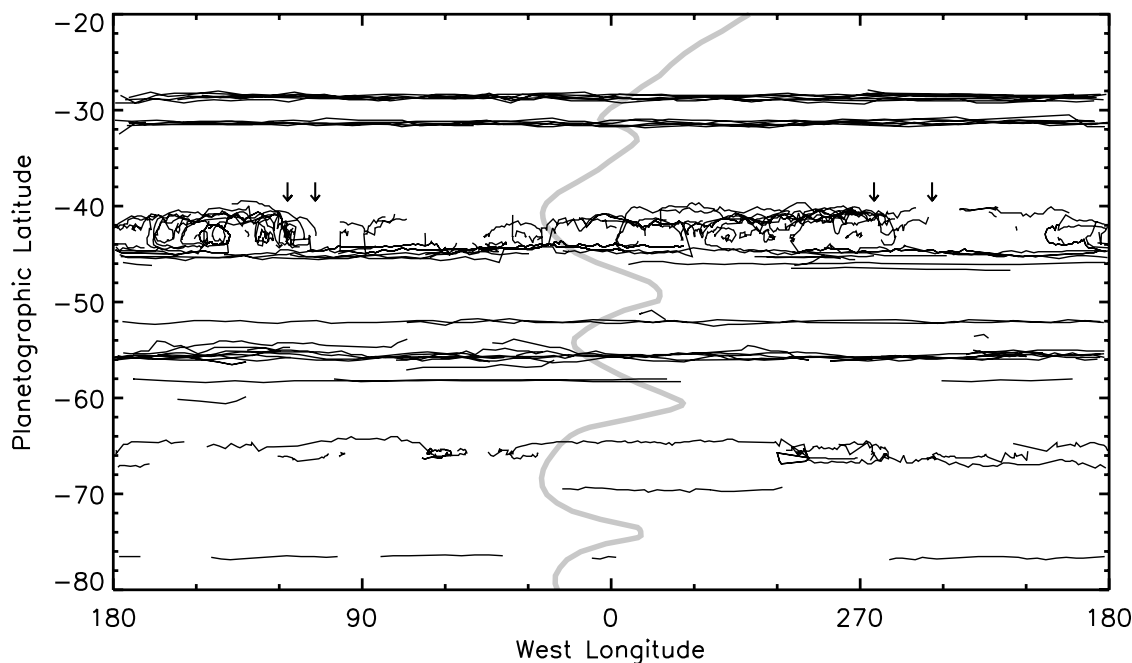
Figure 11. Vortex trajectories during the 95-day approach movie. Each curve represents the trajectory of one of 123 vortices. The thick curve represents the zonal winds measured in this study. Arrows point to the locations of convective storms observed at $41°-6742°$S over the course of the approach movie.

[30] Figure 11 is a plot of the trajectories of the 123 vortices tracked within the AMs. Vortices were observed to drift with both eastward and westward velocities relative to System III. In addition, the AM reveals many changes in drift rate and/or direction, sometimes associated with a vortex-vortex interaction or merger (see section 4.6). In all cases the instantaneous drift rate was indistinguishable from the zonal wind speed at the latitude corresponding to the vortex center. In other words, changes in vortex drift rate were accompanied by changes in vortex latitude and vice versa (following the latitudinal profile of zonal wind). The largest vortex in our study sits alone in its latitude band at 51.8°S and drifted steadily at 50 ± 5 m s^{-1} during the AM. It is tempting to speculate that this vortex is Anne's Spot from the Voyager era [*Sánchez-Lavega et al.*, 2000]. If so, it has moved $\sim 2°$ north in latitude and increased in velocity by ~ 25 m s^{-1}, just as predicted by the zonal wind profile (in addition, its east-west diameter has increased from 3200 km to 4500 km).

[31] Figure 11 dramatically shows the correlation between vortex activity just south of the 41°S jet and the occurrence of convective storms. Vortices in this region tend to drift westward with the ambient wind. Many trajectories originate at the locations where convective storms were observed. On the basis of this observation, *Porco et al.* [2005] speculated that upwelling plumes deposit anticyclonic vorticity at cloud level, spawning vortices. Others analyzing Voyager images of an upwelling near 41°N compared the visual appearance to that of a vertical obstacle in a horizontal flow; vortices are shed in the plume's wake as in a classical Karman vortex street [*Smith et al.*, 1982; *Godfrey et al.*, 1983]. The latter hypothesis would predict the generation of equal numbers of vortices of each sense of vorticity. While we are not able to measure the tangential velocity of individual vortices, vortices generated in this region behave as if they are predominantly anticyclonic, based on their interactions (e.g., orbiting) and stability within a zone of anticyclonic shear in the ambient wind. However, the storm that occurred during the HRM sequence (depicted in Figure 5 of *Porco et al.* [2005]) is associated with the sudden appearance of dark anticyclones as well as a bright vortex that may be a cyclone (based on its similar appearance to vortices in cyclonic shear zones and an indefinite observation of its rotation by the present authors). Future Cassini observations may be able to better test these ideas.

4.4. Appearance of Vortices at Other Wavelengths

[32] We can use the spectral coverage within the HRM data set to make some qualitative statements about the vertical structure of the vortex types described above (also see a similar discussion in section 3). Note that the vortex types are named according to their appearance in CB2 images. Figures 5a and 5b show that dark vortices are also dark in BL1 and MT1 maps, and are not detected at other wavelengths, consistent with low aerosol opacity (or perhaps dark coloration) at the deeper levels sensed by those filters, and no impact on the aerosol distribution or wind field at higher levels. Dark vortices with bright margins retain that appearance in BL1 and MT1 maps. The largest examples increase further in relative brightness in MT2 or MT3 maps, and appear dark (and larger) in UV3 maps. This pattern suggests upwelling and/or upward displacement of horizontal flow at higher levels, a phenomena that is associated with larger anticyclones (nominally high-pressure centers).

[33] Bright-centered vortices appear progressively brighter (relative to surroundings) in MT1, MT2, and

MT3 maps. Although they are embedded within cyclonic shear zones, this spectral pattern is similar to that of anti-cyclones. Vortices may exist in shear zones of the opposite sense of vorticity, but only if sufficiently strong; no such vortices have been documented on the giant planets (and we were not able to directly measure the vortex rotation). Those closest to the pole are also bright in the BL1 maps. The two bright vortices are rare examples of bright features on the BL1 maps (along with the convective storm and two of our unclassified vortices), but are absent in UV3, MT2, and MT3 maps, suggesting that they are deep but contain higher cloud opacity than their surroundings at that level. Our largest vortex, at 51.8°S, appears bright in UV3 and progressively darker in MT1, MT2, and MT3. This spectral pattern is consistent with its presumed cyclonic vorticity (i.e., that it is a low-pressure center, with downwelling at higher levels). The longitudinally quasiperiodic, anticyclon-ic feature near 29.5°−33°S is relatively bright in MT2 and MT3 maps. In addition, the cloud morphology changes with height; oval-shaped features in CB2 maps become a wavy structure in the MT maps.

4.5. Detections and Disappearances

[34] Of the 123 vortices tracked in the AMs, 91 were initially detected after the first AM. We have classified initial detections into four categories: (1) sudden appearance of a compact vortex in an otherwise featureless region (39), (2) organization of a vortex from existing contrast features (20), (3) development of contrast over an extended area and subsequent organization into a vortex (25), and (4) development of a vortex from turbulence associated with a convective storm (7). Some of the initial detections (of all types, but 1 and 2 in particular) may not represent real vortex creation events, but instead reflect the increasing ability to resolve smaller vortices as the AMs progressed. Nineteen initial detections occurred following data gaps; we cannot be sure how these vortices formed. Of these 19, seven were observed to become more compact over time and are classified as Type 3. The other 12 are classified as Type 1.

[35] There were 60 disappearances during the AMs, classified into three categories: (1) disappearance of a compact vortex (25), (2) gradual disorganization (11), and (3) vortex-vortex merger (24). There were 13 disappearances during data gaps. Of these, one could be confidently classified as type 2; the others are classified as type 1. Of the type 2 disappearances, four occurred shortly after a close interaction (e.g., a near miss) with another vortex, though not all close interactions resulted in vortex disappearances.

4.6. Mergers and Other Vortex Behaviors

[36] There were 24 vortex-vortex mergers in the AMs. A few examples are displayed by *Porco et al.* [2005]. Mergers reduced an initial population of 36 to 12 (some experienced multiple mergers). All but three of the mergers occurred in the band near the 41°S jet. This band has both the largest number of vortices and nearly equal numbers of eastward and westward moving vortices. Both of these factors lead to the high merger rate. In the following text, we present a few brief anecdotes in order to provide an idea of the diversity of vortex behaviors.

[37] 1. Some vortices change latitude with no apparent cause. However, the vortices remained within a single dynamical band (i.e., one sense of latitudinal shear in the zonal wind).

[38] 2. Two vortices in the band near 41°S each experienced four mergers in the AMs.

[39] 3. Three mergers involving larger vortices resulted in the ejection of ephemeral, bright filaments.

[40] 4. Ten of the mergers were facilitated by a change in latitude in one or both of the vortices shortly before the merger.

[41] 5. Five of the mergers were facilitated by a change in direction by one or both of the vortices shortly before the merger.

[42] 6. Nine of the mergers occurred between vortices that were moving toward each other in opposite directions relative to System III.

[43] 7. In some cases, the postmerger vortex had a latitude and drift rate different from those of either premerger vortex. For example, two vortices at 42°S drifting westward at 10 m s^{-1} merged on 19 March, resulting in the ejection of bright filaments, a shift in latitude to 45°S, and a change in drift rate to 20 m s^{-1} by the last AM.

[44] 8. Some mergers are facilitated by a previous mutual interaction of vortices. For example, in the band near 41°S, vortices often circulate around one another in a counter-clockwise direction. It is not clear if the orbiting results from mutual vortex interactions or from the presence of a larger circulation pattern within the band. This behavior contributes to one of the observed four merger sequences described above. The sequence of events can be complex. In one case, two vortices passed each other traveling in opposite directions in a shear zone in which westward velocity increases toward the equator. One was at 40.7°S and traveled westward at 10 m s^{-1}. The other was at 42.3°S and traveled eastward at 5 m s^{-1}. Their mutual interaction deflected the first vortex southward to 42.8°S, changing its drift rate to 0 m s^{-1}. The second vortex was deflected northward to 40°S, increasing its drift rate to westward at 10 m s^{-1}. The second vortex eventually caught up to the first and merged with it.

[45] 9. There are two examples of vortex pairs that are connected by an extended filament (8000 km in one case) after passing close to one another (Figure 7).

4.7. Lifetime-Size Relationship

[46] Figure 12 shows the relationship between lifetime and size for nonmerging vortices in the AMs. Considerations of vortex lifetimes contain some ambiguity due to the increasing ability to detect small vortices as the AMs progressed. The populations of vortices that were long-lived (i.e., not observed to appear, merge, nor disappear within the AMs) have a size distribution that is distinct from the short-lived vortices (i.e., observed to both appear and disappear within the AMs). The 11 long-lived, nonmerging vortices ranged in diameter from 1300 to 4500 km (and include the largest vortex observed in the AMs). The 33 short-lived vortices were all <1100 km in diameter. The 43 vortices whose initial detection or disappearance was captured within the AMs, but not both, ranged in size up to 2300 km. These lifetimes are lower limits. Our analysis suggests a positive correlation between lifetime and vortex
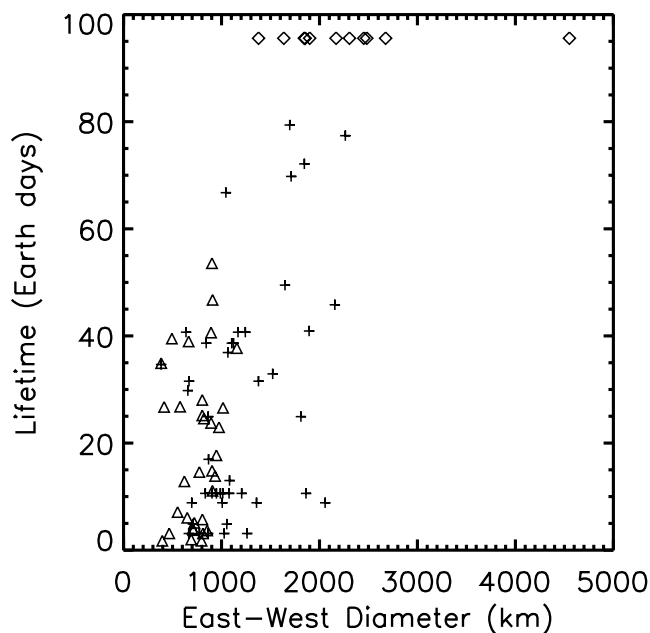
Figure 12. Distribution of vortex lifetimes and sizes. Lifetimes in Earth days are categorized into three groups. Vortices with lifetimes shorter than the 95-day AM sequence are indicated with triangles. Vortices with lifetimes longer than the AM sequence are indicated with diamonds. Pluses indicate vortices that either appeared or disappeared during the approach movie (but not both). Their lifetimes are lower limits. Vortices that merged are excluded from consideration.

size, as is observed on Jupiter [e.g., *Morales-Juberías et al.*, 2002].

[47] There are 18 additional vortices with lifetimes greater than the AM sequence if those with mergers are counted (the lifetime of the merged vortex is appended to the lifetimes of each of the premerger vortices). These 18 experienced at least one merger, leaving nine in last of the AMs with diameters ranging from 1500 to 3000 km.

5. Discussion

[48] Our survey of Saturn's southern hemisphere reveals some striking similarities with the northern hemisphere observed by Voyager [*Smith et al.*, 1981, 1982; *Sromovsky et al.*, 1983; *Ingersoll et al.*, 1984; *Sánchez-Lavega et al.*, 2000]. These similarities include the types and latitudes of certain features as well as the pattern of zonal jets. The region near the westward jet at ∼41° latitude is the most active in both hemispheres, displaying the largest number of small vortices and bright, expanding, convective storms. Similar vortex-storm interactions have been described in each hemisphere. While polygonal wave structures are observed at high latitudes in both hemispheres, the northern polar hexagon is more pronounced, complete in longitude, and longer lived. Voyager analyses noted several major vortices in each hemisphere. The largest nonpolar vortices measured in Voyager images are larger (6000 km east-west diameter) than the largest measured in our study (4500 km). Our largest vortex resembles the Voyager era Anne's Spot in its morphology and location, but is 2° farther north and ∼40% larger in diameter.

[49] Comparing the observed dynamics of Saturn and Jupiter [e.g., *Vasavada and Showman*, 2005] proves interesting. Both planets exhibit a pattern of zonal jets that approach or exceed the barotropic stability criterion for two-dimensional flows at several westward maxima. Convective storms occur on both planets with similar characteristics: they are very small compared to the disk, actively produce cloud material for a period of days to weeks, and are relatively rare (only one or a few occur in a given latitude band, at a given time). Lightning associated with Jovian storms has been noted in nearly every region of cyclonic shear in the zonal winds, and nowhere else [*Little et al.*, 1999; *Dyudina et al.*, 2004]. It occurs near the center of cyclonic regions at lower latitudes, and nearer to the peaks of the westward jets at higher latitudes. Storms on Saturn have been observed near 41° latitude in each hemisphere. In our study, we located the storm centers near the peak of a westward jet.

[50] A significant difference is the abundance of vortices and other dynamical features on Jupiter, compared with the relatively sparse appearance of Saturn (with the caveat that features on Saturn are harder to detect). Jovian vortices cover nearly all the surface area at high northern latitudes, while on Saturn there is no obvious trend in number with latitude. On each planet the largest vortex sits alone within its latitude band. However, Jupiter's Great Red Spot is an anticyclone, while Saturn's largest vortex (in the southern hemisphere, at least) is in a cyclonic shear zone. Jupiter displays a distinct cyclone-anticyclone asymmetry, in that large cyclones exhibit less spatial coherence and become multilobed or extended "conveyor belt" structures. Both cyclones and anticyclones of all sizes on Saturn are compact, and are either round or oval-shaped. There appear to be no Saturn analogs for equatorial hot spots or extended cyclonic structures. Furthermore, on Jupiter, there are no analogs for mid to large compact cyclones or high-latitude, polygonal structures. These comparisons will undoubtedly be refined as Cassini reveals Saturn at even higher spatial resolution and over more of its seasonal cycle.

References

Acarreta, J. R., and A. Sánchez-Lavega (1999), Vertical cloud structure in Saturn's 1990 equatorial storm, *Icarus*, *137*(1), 24–33.

Allison, M., D. A. Godfrey, and R. F. Beebe (1990), A wave dynamic interpretation of Saturn's polar hexagon, *Science*, *247*, 1061–1063.

Banfield, D., P. J. Gierasch, M. Bell, E. Ustinov, A. P. Ingersoll, A. R. Vasavada, R. A. West, and M. J. S. Belton (1998), Jupiter's cloud structure from Galileo imaging data, *Icarus*, *135*(1), 230–250.

Barnet, C. D., J. A. Westphal, R. F. Beebe, and L. F. Huber (1992), Hubble Space Telescope observations of the 1990 equatorial disturbance on Saturn: Zonal winds and central meridian albedos, *Icarus*, *100*(2), 499–511.

Beebe, R. F., C. D. Barnet, P. V. Sada, and A. S. Murrell (1992), The onset and growth of the 1990 equatorial disturbance on Saturn, *Icarus*, *95*(2), 163–172.

Belton, M. J. S., et al. (1996), Galileo's first images of Jupiter and the Galilean satellites, *Science*, *274*, 377–385.

Dowling, T. E., and A. P. Ingersoll (1989), Jupiter's Great Red Spot as a shallow-water system, *J. Atmos. Sci.*, *46*(21), 3256–3278.

Dyudina, U. A., A. D. Del Genio, A. P. Ingersoll, C. C. Porco, R. A. West, A. R. Vasavada, and J. M. Barbara (2004), Lightning on Jupiter observed

in the Hα line by the Cassini imaging science subsystem, *Icarus*, *172*(1), 24–36.

Flasar, F. M., et al. (2005), Temperatures, winds and composition in the Saturnian system, *Science*, *307*, 1247–1251.

Godfrey, D. A. (1988), A hexagonal feature around Saturn's north pole, *Icarus*, *76*(2), 335–356.

Godfrey, D. A., and V. Moore (1986), The Saturnian ribbon feature—A baroclinically unstable model, *Icarus*, *68*(2), 313–343.

Godfrey, D. A., G. E. Hunt, and V. E. Suomi (1983), Some dynamical properties of vortex streets in Saturn's atmosphere from analysis of Voyager images, *Geophys. Res. Lett.*, *10*(9), 865–868.

Hunt, G. E., D. A. Godfrey, J.-P. Muller, and R. F. T. Barrey (1982), Dynamical features in the northern hemisphere of Saturn from Voyager 1 images, *Nature*, *297*, 132–134.

Ingersoll, A. P., R. F. Beebe, B. J. Conrath, and G. E. Hunt (1984), Structure and dynamics of Saturn's atmosphere, in *Saturn*, edited by T. Gehrels and M. S. Matthews, pp. 195–238, Univ. of Ariz. Press, Tucson.

Karkoschka, E., and M. Tomasko (2005), Saturn vertical and latitudinal cloud structure 1991–2004 from HST imaging in 30 filters, *Icarus*, *179*(1), 195–221.

Li, L., A. P. Ingersoll, A. R. Vasavada, C. C. Porco, A. D. Del Genio, and S. P. Ewald (2004), Life cycles of spots on Jupiter from Cassini images, *Icarus*, *172*(1), 9–23.

Little, B., C. D. Anger, A. P. Ingersoll, A. R. Vasavada, D. Senske, H. H. Breneman, and W. J. Borucki (1999), Galileo images of lightning on Jupiter, *Icarus*, *142*(2), 306–322.

Morales-Juberías, R., A. Sánchez-Lavega, J. Lecacheaux, and F. Colas (2002), A comparative study of Jovian anticyclone properties from a six year (1994–2000) survey, *Icarus*, *157*(1), 76–90.

Muñoz, O., F. Moreno, A. Molina, D. Grodent, J. C. Gérard, and V. Dols (2004), Study of the vertical structure of Saturn's atmosphere using HST/WFPC2 images, *Icarus*, *169*(2), 413–428.

Orton, G. S., and P. A. Yanamandra-Fisher (2005), Saturn's temperature field from high-resolution middle-infrared imaging, *Science*, *307*, 696–698.

Pérez-Hoyos, S., A. Sánchez-Lavega, R. G. French, and J. F. Rojas (2005), Saturn's cloud structure and temporal evolution from ten years of Hubble Space Telescope images (1994–2003), *Icarus*, *176*(1), 155–174.

Porco, C. C., et al. (2003), Cassini imaging of Jupiter's atmosphere, satellites, and rings, *Science*, *299*, 1541–1547.

Porco, C. C., et al. (2004), Cassini Imaging Science: Instrument characteristics and capabilities and anticipated scientific investigations at Saturn, *Space Sci. Rev.*, *115*(1–4), 363–497.

Porco, C. C., et al. (2005), Cassini Imaging Science: Initial results on Saturn's atmosphere, *Science*, *307*, 1243–1246.

Sánchez-Lavega, A. (2005), How long is the day on Saturn?, *Science*, *307*, 1223–1224.

Sánchez-Lavega, A., F. Colas, J. Lecacheux, P. Laques, I. Miyazaki, and D. Parker (1991), The Great White Spot and disturbances in Saturn's equatorial atmosphere during 1990, *Nature*, *353*, 397–401.

Sánchez-Lavega, A., J. F. Rojas, and P. V. Sada (2000), Saturn's zonal winds at cloud level, *Icarus*, *147*(2), 405–420.

Sánchez-Lavega, A., S. Pérez-Hoyos, J. R. Acarreta, and R. G. French (2002), No hexagonal wave around Saturn's southern pole, *Icarus*, *160*(1), 216–219.

Sánchez-Lavega, A., S. Pérez-Hoyos, J. F. Rojas, R. Hueso, and R. G. French (2003), A strong decrease in Saturn's equatorial jet at cloud level, *Nature*, *423*, 623–625.

Sánchez-Lavega, A., R. Hueso, S. Pérez-Hoyos, J. F. Rojas, and R. G. French (2004), Saturn's cloud morphology and zonal winds before the Cassini encounter, *Icarus*, *170*(2), 519–523.

Smith, B. A., et al. (1981), Encounter with Saturn: Voyager 1 imaging science results, *Science*, *212*, 163–190.

Smith, B. A., et al. (1982), A new look at the Saturn system: The Voyager 2 images, *Science*, *215*, 504–537.

Sromovsky, L. A., H. E. Revercomb, R. J. Krauss, and V. E. Suomi (1983), Voyager 2 observations of Saturn's northern mid-latitude cloud features: Morphology, motions, and evolution, *J. Geophys. Res.*, *88*(A11), 8650–8666.

Temma, T., N. J. Chanover, A. A. Simon-Miller, D. A. Glenar, J. J. Hillman, and D. M. Kuehn (2005), Vertical structure modeling of Saturn's equatorial region using high spectral resolution imaging, *Icarus*, *175*(2), 464–489.

Vasavada, A. R., and A. P. Showman (2005), Jovian atmospheric dynamics: An update after Galileo and Cassini, *Rep. Prog. Phys.*, *68*(8), 1935–1996.

Vasavada, A. R., et al. (1998), Galileo imaging of Jupiter's atmosphere: The Great Red Spot, equatorial region and white ovals, *Icarus*, *135*(1), 265–275.

————————————

A. D. Del Genio, NASA Goddard Institute for Space Studies, 2880 Broadway, New York, NY 10025, USA. (adelgenio@giss.nasa.gov)

S. M. Hörst, A. R. Vasavada, and R. A. West, Jet Propulsion Laboratory, California Institute of Technology, 4800 Oak Grove Drive, Pasadena, CA 91109, USA. (horst@alumni.caltech.edu; ashwin.r.vasavada@jpl.nasa.gov; robert.a.west@jpl.nasa.gov)

A. P. Ingersoll, Division of Geological and Planetary Sciences, California Institute of Technology, Pasadena, CA 91125, USA. (api@gps.caltech.edu)

M. R. Kennedy, Department of Geological Sciences, Arizona State University, Box 871404, Tempe, AZ 85287-1404, USA. (megan.kennedy@asu.edu)

C. C. Porco, Cassini Imaging Central Laboratory for Operations, Space Science Institute, 4750 Walnut Street, Suite 205, Boulder, CO 80301, USA. (carolyn@ciclops.org)